

# Adaptive power-split control design for marine hybrid diesel powertrain

## **Sergey Samokhin \***

Postgraduate researcher  
School of Electrical Engineering  
Aalto University  
Otaniementie 17, 02150  
Espoo, Finland  
Email: sergey.samokhin@aalto.fi

## **Sotiris Topaloglou**

Postgraduate researcher  
School of Naval Architecture  
and Marine Engineering  
National Technical University of Athens  
Zografou Campus-15780, Athens, Greece  
Email: akis@lme.ntua.gr

## **George Papalambrou**

Assistant professor  
School of Naval Architecture  
and Marine Engineering  
National Technical University of Athens  
Zografou Campus-15780, Athens, Greece  
Email: george.papalambrou@lme.ntua.gr

## **Kai Zenger**

Senior lecturer  
School of Electrical Engineering  
Aalto University  
Otaniementie 17, 02150  
Espoo, Finland  
Email: kai.zenger@aalto.fi

## **Nikolaos Kyrtatos**

Professor  
School of Naval Architecture  
and Marine Engineering  
National Technical University of Athens  
Zografou Campus-15780, Athens, Greece  
Email: nkyrt@lme.ntua.gr

*It is known that mechanical wear and tear of components of large marine engines throughout their lifetime can cause the engine dynamics to alter. Since traditional control systems with fixed parameters cannot deal with this issue, the engine performance may degrade. In this work, we introduce adaptive control algorithms capable of adapting the control system in order to preserve the engine performance once its dynamics deviate from the nominal ones. Particularly, direct and indirect model reference adaptation mechanisms are studied. In this work, the case of degraded oxygen sensor is investigated as an example of engine components deterioration throughout its lifetime. The controllers are implemented in Simulink and their performance is evaluated under both nominal and degraded sensor conditions. Specifically, the sensor degradation is imitated by altering its time-delay. In such conditions, adaptive controllers demonstrate a notable improvement in tracking performance compared to the fixed parameters PI controller. Finally, the designed controllers are validated on the hybrid marine engine testbed using dSpace rapid prototyping system.*

## **1 Introduction**

During the last decades, marine diesel engine emission regulations have become increasingly stringent due to stricter environmental requirements imposed by the International Maritime Organization (IMO) [1]. As a result, achievement of near-zero emissions has recently become one of the key targets for marine engine manufacturers [2,3].

Recently, the combination of an internal combustion engine with an electric motor has emerged as a powerful approach for reducing emissions within the automotive industry [4]. A large number of research papers has been devoted to evaluating various aspects of hybrid electric vehicles (HEVs), including components sizing, control systems design and topologies investigations. The control of HEVs is usually categorized into rule- and optimization-based algorithms [5]. Various optimization-based algorithms have been proposed for HEVs control, including model-predictive control [6], optimal control based on Pontryagin's minimum principle [7,8], and genetic algorithms [9]. Typ-

---

\*Corresponding author

ically, these algorithms solve a constrained optimal control problem aimed at minimizing engine fuel consumption, resulting in a globally optimal controller [4].

However, such optimization-based control algorithms rely on fixed parameters and therefore provide a global optimum only in the nominal case, i.e. the case for which they were designed [5]. Moreover, mechanical wear and tear of power-train components throughout the vehicle lifetime may cause its dynamics to change, leading to the non-optimized use of power, since the optimal tuning of control systems differs for new and worn-out engines [10,11].

This problem becomes more critical in the marine industry, as large-scale marine diesel engines are typically customized for each individual customer and are therefore produced in very limited quantities. Together with high running costs, this prevents thorough tuning and testing which is, for example, available in the automotive industry, where engines are mass-produced [12]. Moreover, since engines mounted on large vessels are more difficult to maintain, the control systems must be designed sufficiently robust to deal with engine dynamics variation. Such variation can occur, for example, due to severe operating conditions or aggressive load transients (e.g., sailing through rough seas).

Many papers have addressed the problem of control system adaptation to varying engine dynamics in the automotive industry. These include classical adaptive controllers [13], adaptive model predictive controllers (MPC) [14] and controllers based on neural network (NN), including self-tuning NN based control [15], adaptive NN based MPC [16] and fuzzy NN based sliding mode controller [17]. To the authors' knowledge little research has been published on the problem of control system adaptivity within the marine industry [18].

Hybridization in the marine industry is a relatively new area with little research available. One of the problems concerning hybrid marine engines is the absence of energy recuperation via braking, which is defined by the marine driving cycle [19]. Driving cycles typical for the applications in the marine and automotive industries have been compared in [19], which showed that the typical speed profile of a cruise ferry, unlike that of a city car, is almost constant over a large time-interval, with few speed fluctuations. Hence, braking energy is effectively absent for recovery. Nevertheless, the motivation for use of hybrids in marine applications is to unload the engine at high loads, especially during aggressive load transients, in order to minimize emissions [19]. In addition, propulsion engines installed on cruise ferries are typically coupled to so-called shaft generators, thus forming hybrid powertrain [20,21]. Such generators are typically used to supply the electricity for the entire ship (power take out (PTO) mode) and to improve the maneuverability of the vessel (power take in (PTI) mode). Therefore, the control topology proposed in this article would only re-

quire a proper power-split control system rather than the whole powertrain redesign, resulting in a low-cost implementation.

In order to achieve the control target of unloading the engine at high loads and during transients, the appropriate engine parameter needs to be chosen for describing the current engine operation. In the case of modern diesel engine, this parameter is the air-fuel ratio (AFR), since it directly correlates with the engine-out emissions (e.g., NO<sub>x</sub>, particulate matter) and current load, and is easily available with an on-board standard sensor [22]. AFR can therefore be considered a suitable cost for control purposes. Thus, controlling the torque supply from the electric motor can allow the AFR to be regulated to a set-point, thereby reducing emissions. We note that there exist a variety of technologies (e.g., variable geometry turbocharging (VGT), turbines with wastegate, exhaust gas recirculation (EGR)) aimed at reducing diesel engines emissions by means of AFR regulation. However, these affect the combustion mixture directly by means of intake air regulation or exhaust gas recirculation, while the proposed PTI topology utilizes extra available electricity to reduce the loading of the propulsion engine. Thus, the in-cylinder gas composition is still affected, but indirectly via load moderation. Therefore, the proposed topology can be utilized in a combination with the existing more standard AFR regulation techniques to provide additional degrees of freedom for the emissions reduction.

In this work, the goal is to design and compare direct and indirect adaptive control algorithms capable of adapting the control system to varying dynamics of the hybrid marine diesel engine. We demonstrate the benefits of such adaptive control concepts usage by comparing the experimental results of the hybrid power train control under nominal (or design) and deteriorated sensor conditions. The deteriorated sensor is imitated by altering the time-delay of the universal exhaust gas oxygen (UEGO) sensor, as it is known that the measurement delay can cause adverse effect on the closed-loop control system. We also compare the performance of the adaptive controllers with a conventional fixed parameters control (FPC) strategy, such as the proportional-integral (PI) controller, in order to evaluate the feasibility of the proposed control approaches. First, the proposed control system is evaluated via simulations in Matlab/Simulink using the validated hybrid engine model. The controllers are tuned, and their performance is evaluated with the nominal and altered system dynamics. Thereafter, the controllers are deployed on the testbed, and their performance is confirmed experimentally.

This paper is structured as follows. In Section 2 the hybrid engine setup is presented, the first-principles model is developed and validated. The adaptive controllers are described in detail in Section 3. The numerical simulation of the adaptive lambda controllers

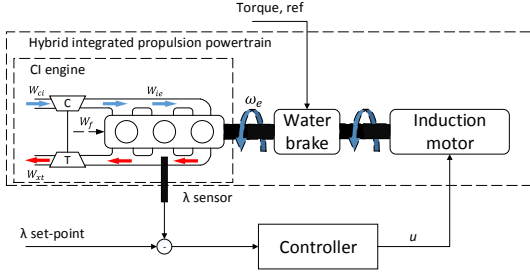


Fig. 1. Lambda control diagram of the hybrid integrated propulsion powertrain. C - compressor, T - Turbine. The lambda sensor placement is shown schematically (located downstream the turbine in real setup).

is done in Section 4. The developed controllers are validated with on-engine tests in Section 5 and the work is concluded in Section 6.

## 2 System description and modeling

Fig. 1 shows the block-diagram of the hybrid integrated propulsion powertrain (HIPPO) closed-loop lambda control configuration. The HIPPO is composed of three main parts: Caterpillar 3176B marine diesel engine (6 cylinders, 448 kW at 2300 rpm), water-brake dynamometer (1200 kW) and auxiliary induction motor (110 kW). The key powertrain characteristics are listed in Tab. 1.

The high-speed turbocharged diesel engine is linked to the dynamometer and the water-brake via cardan shaft. Depending on the test mode, the water-brake dynamometer can provide a step-wise or a “propeller” type of load. This way, we can imitate various applications of hybrid marine engines, including those for ship propulsion and on-board electricity generation. The propeller curve loading is, for example, typical when the engine acts as a propulsion unit, while the step-wise loading characterizes the generator mode (or the auxiliary type engine) [23]. In order to provide the desired load on the engine, the water-brake torque is controlled in closed-loop using the specifically designed robust  $H_\infty$  controller. The modeling of the water brake is outside the scope of this work, as the real torque curves are used as the inputs for the powertrain numerical simulations.

The induction motor is linked to the water-brake directly to form a parallel hybrid engine configuration and a frequency inverter is used to regulate the torque output of the motor. The torque control mode is used for the AC motor control and the rotational speed is defined solely by the diesel engine. In our setup, the induction motor is powered directly from the grid. Although, in real marine application this would not be feasible and a proper energy storage system would be required, our test facility serves different purposes. The main goal here is to evaluate the possibility of transient control of emissions, as well as to assess the feasi-

bility of the adaptive control algorithms.

In this section, a control-oriented model of the hybrid engine is developed, simple but capable of catching the dynamics in the variables of interest, i.e. lambda, speed and torque. Modeling by the first principles is used in this work. Initially more tedious, theoretical modeling pays off at later stages of the model-based control design, providing more information about the system and reducing the need of numerous plants, identified at various engine operating points.

The standard mean value modeling technique is used to model air and fuel path of the diesel engine [24–27]. The nonlinear model of the hybrid propulsion powertrain is implemented in Matlab/Simulink.

### 2.1 Induction motor model

The dynamics of the electromagnetic torque produced by the AC motor are nearly instantaneous in comparison to the diesel engine. Furthermore, the input to torque behavior of the motor is essentially linear which allows us to simplify the model without compromising the data fit. Therefore, a linear transfer function model of the form

$$\frac{M_{ac}}{u_{cmd}} = \frac{K}{\tau_{ac}s + 1} \quad (1)$$

can be used, where  $M_{ac}$  (Nm) is the motor torque and  $u_{cmd}$  (V) is the frequency inverter command. The gain  $K$  and the time-constant  $\tau_{ac}$  are chosen such, that a good match with the experimental data is achieved.

### 2.2 Air-path system model

A simple third-order model of combustion engine airpath was proposed and validated in [28]. In our work, a few modifications to the existing model have been done in order to improve the match with the experimental data. The model is briefly summarized hereafter. The time-dependency ( $t$ ) in the modeling equations is omitted for clarity. The intake and exhaust pressures are defined by the ideal gas law and the mass balance, while the turbocharger power — by the power transfer between the compressor and the turbine

$$\dot{p}_i = \frac{R_i T_i}{V_i} (W_{ci} - W_{ie}) \quad (2a)$$

$$\dot{p}_x = \frac{R_x T_x}{V_x} (W_{ie} + W_f - W_{xt}) \quad (2b)$$

$$\dot{p}_c = \frac{1}{\tau_c} (\eta_t P_t - P_c), \quad (2c)$$

where  $R$  ( $\text{J}\cdot\text{kg}^{-1}\text{K}^{-1}$ ),  $T$  (K) and  $V$  ( $\text{m}^3$ ) denote the specific gas constant of the air, its temperature and the manifold volume, respectively. The subscripts stand

Table 1. Engine and motor characteristics

Type	Caterpillar 3176B marine diesel engine
General data	In-line 6 cylinders, 4-stroke, 10.3 L
Power	448 kW @ 2300 rpm
Torque (limited)	500 Nm
Type	Induction motor
Torque	250 Nm
Inverter control command	0...0.1 V

for the following engine components:  $i$  for the intake manifold,  $x$  for the exhaust manifold,  $f$  for fuel,  $c$  for the compressor and  $xt$  for the turbine. The effect of the temperature derivatives  $\dot{T}_i$  and  $\dot{T}_x$  on  $\dot{p}_i$  and  $\dot{p}_x$  is neglected, however, temperatures  $T_i$  and  $T_x$  itself are not assumed constant (quasi-static approach) [25].

The compressor power  $P_c$  (W) is related to the temperature across it and the air mass flow as

$$P_c = W_{ci} c_p (T_i - T_a), \quad (3)$$

where  $c_{p,i}$  ( $\text{J}\cdot\text{kg}^{-1}\text{K}^{-1}$ ) is the gas specific heat capacity in constant pressure and  $T_a$  (K) is the ambient temperature.

Under assumption of the isentropic compression we know that  $\frac{T_{i, is}}{T_a} = \left(\frac{p_i}{p_a}\right)^{\frac{\gamma-1}{\gamma}}$ . The efficiency of the compressor is based on the temperature increase across it

$$\eta_c = \frac{T_{i, is} - T_a}{T_i - T_a}, \quad (4)$$

where  $T_{i, is}$  is the isentropic compressor temperature. Combining the above expressions, the temperature at the compressor output can be expressed as

$$T_i = T_a \left(1 + \frac{1}{\eta_c} \left(\left(\frac{p_i}{p_a}\right)^\mu - 1\right)\right). \quad (5)$$

The equation for compressor mass flow is obtained by inserting Eqn. 5 into Eqn. 3

$$W_{ci} = \frac{\eta_c P_c}{T_a c_{p,i} \left(\left(\frac{p_i}{p_a}\right)^{\mu_c} - 1\right)}, \quad (6)$$

where  $p_a$  (Pa) is the ambient pressure,  $\mu_c = (\gamma_c - 1)/\gamma_c$  and  $\gamma_c = c_{p,i}/c_{v,i}$ .

The turbine power equation  $P_t$  is written similar to Eqn. 3 as

$$P_t = W_{xt} c_p T_x \left(1 - \left(\frac{p_a}{p_x}\right)^{\mu_x}\right). \quad (7)$$

It has been observed that the model match with the experimental data is greatly improved by approximating the exhaust temperature as a function of the normalized AFR or  $\lambda$  [26]

$$T_x = T_i + a_{t1} \lambda^{a_{t2}} + a_{t3}, \quad (8)$$

where the coefficients  $a_{t1}$ ,  $a_{t2}$  and  $a_{t3}$  are used as tuning parameters.

The mass flow  $W_{ie}$  from the intake manifold into the cylinders is based on the engines capacity to pump the air

$$W_{ie} = \frac{V_d \omega_e p_i}{v 2\pi R_i T_i} \eta_v(\omega_e), \quad (9)$$

where  $V_d$  ( $\text{m}^{-3}$ ) is the engine displacement volume and  $v = 1$  for four-stroke engines. The engine volumetric efficiency  $\eta_v$  depends on several variables, but can be approximated well by the quadratic function of the engine speed  $\omega_e$  (rad/s) [26]

$$\eta_v = a_{v1} + a_{v2} \omega_e + a_{v3} \omega_e^2, \quad (10)$$

where the coefficients  $a_{v1}$ ,  $a_{v2}$  and  $a_{v3}$  are used as tuning parameters.

The turbocharger has a fixed geometry without a wastegate and is, therefore, fitted for the entire engine operating range. Hence, the mass flow  $W_{xt}$  through the turbine can be modeled using the orifice flow equation [29]

$$W_{xt} = \frac{A_t}{\sqrt{R_x T_x}} p_x \Psi \left(\frac{p_a}{p_x}\right), \quad (11)$$

where  $A_t$  ( $\text{m}^2$ ) is the constant turbine effective area and  $\Psi \left(\frac{p_a}{p_x}\right)$  is the flow correction coefficient

$$\Psi \left(\frac{p_a}{p_x}\right) = \begin{cases} \sqrt{\frac{2\gamma}{\gamma-1} \left(\left(\frac{p_a}{p_x}\right)^{\frac{2}{\gamma}} - \left(\frac{p_a}{p_x}\right)^{\frac{\gamma+1}{\gamma}}\right)} & \text{if } \left(\frac{p_a}{p_x}\right) > r_c \\ \gamma^{\frac{1}{2}} \left(\frac{2}{\gamma+1}\right)^{\frac{\gamma+1}{2(\gamma-1)}} & \text{if } \left(\frac{p_a}{p_x}\right) \leq r_c \end{cases}$$

where the critical pressure ratio is defined as  $r_c = \left(\frac{2}{\gamma+1}\right)^{\frac{\gamma}{\gamma-1}}$ .

### 2.3 Fuel-path system model

The mean acceleration of the crankshaft is computed from the torque balance equation, which includes four terms. Apart from the engine indicated  $M_e$ , friction  $M_{fr}$  and water-brake (or load)  $M_l$  torque, an induction motor torque  $M_{ac}$  is taken into account. This yields

$$\dot{\omega}_e = \frac{M_e + M_{ac} - M_{fr} - M_l}{J}, \quad (12)$$

where  $J$  (kg·m<sup>2</sup>) is the engine moment of inertia. The simplified equation for the mean engine indicated torque  $M_e$  is written under the assumption that the engine indicated thermal efficiency  $\eta_i$  is a function of speed and lambda

$$M_e = \frac{W_f H_i}{\omega_e} \eta_i(\omega_e, \lambda), \quad (13)$$

where  $H_i$  (MJ/kg) is the lower heating value of the fuel and  $\eta_i = (a_1 + a_2 \omega_e + a_3 \omega_e^2)(1 - a_4 \lambda^{a_5})$  (see [26]).

The friction losses in the engine (e.g., pumping, resistance between the piston rings, piston skirt and cylinder wall, friction in crankshaft bearings, gears) are accounted by introducing the friction torque  $M_{fr}$  as [29]

$$M_{fr} = \frac{f_{mep} V_d}{2\pi v}, \quad (14)$$

where the friction mean effective pressure  $f_{mep}$  (kPa) is approximated with the experimental equation [29]

$$f_{mep} = C1 + 48(N_e/1000) + 0.4\bar{S}_p^2,$$

where  $C1 = 75$  kPa is the constant,  $\bar{S}_p = 2SN_e/60$  is the mean piston speed (m/s),  $S$  is the stroke (m) and  $N_e$  is the engine rotational speed (rpm).

The crank rotational speed  $\omega_e$  is closed-loop controlled by the engine built-in control mechanism which continuously adjusts the amount of fuel  $W_f$  injected into the cylinders.

The water-brake torque  $M_l$  is regarded as the external disturbance in the simulations.

### 2.4 Relative air-fuel ratio definition

The controllable output of the hybrid powertrain is the relative AFR  $\lambda$  that defines the air-fuel ratio normalized by the stoichiometric constant  $\lambda_s$

$$\lambda = \frac{W_{ie}}{W_f} \cdot \frac{1}{\lambda_s} \quad (15)$$

The latter equation shows that  $\lambda$  is affected by the variables generated by the two engine subsystems, namely air and fuel paths. Obviously, accurate models of these subsystems should provide a good match between measured and simulated  $\lambda$ . The measurements performed on the engine testbed have shown that the AFR has a considerable time-delay  $\tau_\lambda = 0.79$  sec which is explained by the exhaust gas transport delay due to the UEGO sensor placement. This delay needs to be included into the model, as it is known that time-delays can have an adverse effect on control systems. Taking the delay into account in early stages of the control design will allow to properly tune the controller and study the potential instability issues.

We note that apart from the sensor location, the time-delay is governed by the engine speed, to which it is inversely proportional. Although the dependency between the speed and delay is not investigated separately, the case of increased time-delay is covered by the simulation and experimental studies.

### 2.5 Model implementation and validation

The developed control-oriented model of the hybrid powertrain is implemented in Simulink, as it is then easy to download the designed controller to the Dspace engine control board for rapid prototyping. The fixed-step discrete-time solver with the sampling time  $t = 0.01$  sec is used during the simulation.

The parameters estimation and the subsequent model validation is done using the experimental data from the HIPPO testbed. For this purpose its dynamics were excited using the pseudorandom binary sequence (PRBS) excitation input to the frequency inverter and the time-domain transient data for  $\lambda$ ,  $\omega_e$ ,  $M_e$  and  $M_l$  was recorded.

The constructed model contains a number of parameters that are not known precisely and/or cannot be measured. Therefore, these are estimated using the Matlab parameter estimation toolbox and then fine-tuned manually to obtain the best data fit. These parameters include:  $a_{v1}$ ,  $a_{v2}$ ,  $a_{v3}$ ,  $\eta_c$ ,  $\eta_t$ ,  $A_t$ ,  $a_1$ ,  $a_2$ ,  $a_3$ ,  $a_4$  and  $a_5$ . The data-set 1 for the diesel engine speed, lambda and torque used in the parameter estimation is shown in Fig. 2 and Fig. 3 (top). The PRBS excitation signal is also shown in Fig. 3 (bottom).

The model is verified with the data-set 2 obtained at another engine operating point where the engine speed and torque were varied simultaneously according to the propeller curve profile (see Fig. 4). The torque profiles for measured and simulated data as well as the frequency inverter control command are demonstrated in Fig. 5.

The quality of the model is assessed using the root mean square (RMS) error

$$RMSE = \sqrt{\frac{\sum_{i=1}^N (\hat{y}_i - y_i)^2}{N}},$$

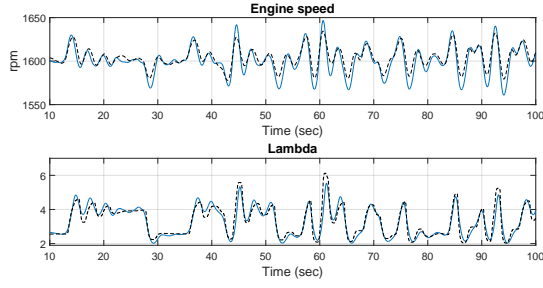


Fig. 2. Model parameter estimation. Measured and simulated data for the engine speed and lambda. Legend: — simulated, - - - measured.

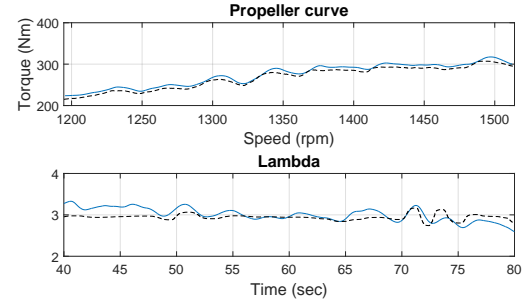


Fig. 4. Model validation with the mild propeller curve. Measured and simulated data for the engine torque and lambda. Legend: — simulated, - - - measured.

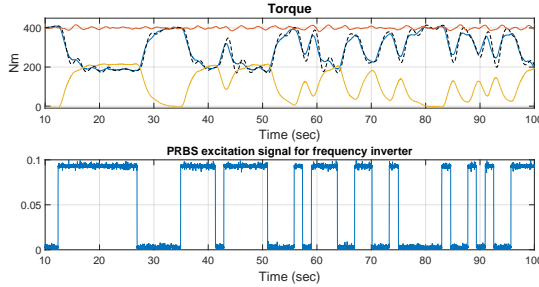


Fig. 3. Model parameter estimation. Measured and simulated data for the engine torque. Water-brake and induction motor torque profiles as well as the PRBS excitation signal for frequency inverter are also shown. Legend (top plot): — simulated diesel torque, - - - measured diesel torque, — measured motor torque, — measured load torque.

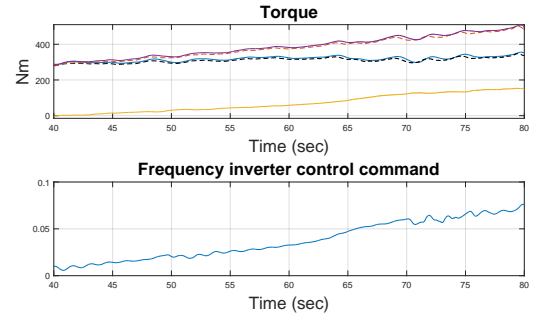


Fig. 5. Model validation with the mild propeller curve. Measured and simulated data for the engine torque. Water-brake and induction motor torque profiles as well as the commanded signal for the frequency inverter are also shown. Legend (top plot): — simulated diesel torque, - - - measured diesel torque, — measured motor torque, - - - measured load torque, — simulated total powertrain torque.

where  $\hat{y}$  and  $y$  are the modeled and measured outputs, respectively and  $N$  is the amount of measurement points. The RMS error values for the engine speed, lambda and torque on the estimation and validation data-sets are shown in Tab. 2. It can be seen that the RMS errors for the estimation data-set 1 are small compared to the mean values of the respective data, indicating sufficiently good model fit. Tab. 2 also shows that the RMS error of the engine speed on the validation data-set 2 increases, whereas the RMS errors for torque and lambda remain low.

The conclusion can be drawn that the mean value model of the hybrid powertrain behaves equally well at various engine operating points and can be therefore utilized for further control design and tuning procedures.

### 3 Adaptive power split controller design

In this section we introduce and further design the *direct* and *indirect* versions of the well-known model reference adaptive control (MRAC) algorithm. In both of these control approaches the desired dynamical plant behavior is defined by the reference model. We exemplify the application of the first-order reference model with the direct adaptation scheme and the

second-order model with the indirect scheme. For more details on the MRAC algorithms the reader is referred to [30,31]. In addition, the baseline PI controller is designed to support the need of more advanced algorithms.

#### 3.1 Direct output error adaptive control

The direct adaptive control algorithm can be thought of as a simplified version of indirect adaptive control, since the controller parameters are directly identified from the process, i.e. the identifier and control parameters are identical. Fig. 6 shows a block diagram of the direct adaptive control scheme and its structure is summarized hereafter.

The core of the algorithm is the error

$$e_0 = y_p - y_m$$

between the plant and the reference dynamical model outputs  $y_p$  ( $\lambda$  in our case) and  $y_m$ , respectively. The key property of the direct adaptation is that the stability and asymptotic tracking can be guaranteed only if

Table 2. Root mean square error (RMSE) of the modeled lambda, speed and torque during the estimation and validation.

		Diesel torque (Nm)	Engine speed (rpm)	Lambda
Data-set 1	Mean	289	1605	3.31
	RMSE	18	7	0.28
Data-set 2	Mean	286	1491	3.16
	RMSE	12	19	0.28

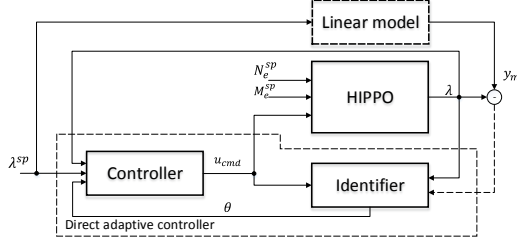


Fig. 6. Direct adaptive control algorithm block-diagram. Designations:  $N_e^{sp}$  — engine speed set-point,  $M_e^{sp}$  — load torque set-point.

the plant is minimum-phase [31]. Based on the experimental data for lambda transient response (see Fig. 2) it can be confirmed that our plant is indeed minimum-phase. Therefore, under this assumption, the stable model is chosen to be minimum phase, with the numerator  $n_m(s)$  and denominator  $d_m(s)$  being both monic and coprime polynomials and the gain  $k_m > 0$ . Assuming that the plant behavior can be represented well by the first-order dynamics ( $n = 1$ ), the model is chosen as

$$\frac{y_m}{r} = \frac{k_m}{s + a_m},$$

where  $r$  is the reference value and  $a_m$  is a positive constant. In general, the controller structure involves the filters for the input  $\dot{\mathbf{w}}^{(1)} = \mathbf{E}\mathbf{w}^{(1)} + \mathbf{b}_\xi u$  and the output  $\dot{\mathbf{w}}^{(2)} = \mathbf{E}\mathbf{w}^{(2)} + \mathbf{b}_\xi y_p$  [30], however the design parameters  $\mathbf{E} \in \mathbb{R}^{(n-1) \times (n-1)}$  and  $\mathbf{b}_\xi \in \mathbb{R}^{(n-1)}$  vanish when  $n = 1$ , thus simplifying the controller structure.

In addition, the vector of controller parameters  $\boldsymbol{\theta}(t)$  and the vector of signals  $\mathbf{w}(t)$  are reduced to

$$\boldsymbol{\theta}(t) = [c_0(t) \ d_0(t)]^T \quad \mathbf{w}(t) = [r(t) \ y_p(t)]^T,$$

where  $c_0(t)$  and  $d_0(t)$  are the time-varying parameters (no physical interpretation) used for the control law calculation. Due to the limits enforced by the frequency inverter, the control signal is calculated as

$$\begin{cases} u = u_{min} & \text{if } u \leq u_{min} \\ u = \boldsymbol{\theta}^T \mathbf{w} & \text{if } u_{min} < u < u_{max} \\ u = u_{max} & \text{if } u \geq u_{max} \end{cases} \quad (16)$$

The gradient decent algorithm is used to adapt the control parameters

$$\dot{\boldsymbol{\theta}} = -ge_0 \mathbf{w},$$

where  $g$  is the tuning parameter. In order to improve the robustness and solve the saturation problem two update law modifications have been done:

1. **Leakage term.** This modifies the parameter update law to prevent the parameters drift into the instability region [30]

$$\dot{\boldsymbol{\theta}} = -ge_0 \mathbf{w} - \sigma \boldsymbol{\theta},$$

where  $\sigma > 0$  is a small constant used to keep  $\boldsymbol{\theta}$  bounded.

2. **Anti-windup mechanism.** This is a “dead-zone”-like update law modification which stops the adaptation, once the control signal gets saturated. The control signal saturation error is defined as  $e_a = u_{sat} - u$ , where  $u_{sat}$  is the saturated control signal entering the plant and  $u$  is the signal generated by the controller. The update law is modified as

$$\begin{cases} \dot{\boldsymbol{\theta}} = -ge_0 \mathbf{w} - \sigma \boldsymbol{\theta} & \text{if } |e_a| \leq \gamma \\ \dot{\boldsymbol{\theta}} = 0 & \text{if } |e_a| > \gamma, \end{cases}$$

where  $\gamma$  is chosen small enough to stop the adaptation when saturation occurs.

### 3.2 Indirect adaptive (self-tuning) control

In this method a clear distinction is done between the controller and plant parametrization. Fig. 7 shows the block diagram of the indirect adaptive control algorithm. In this subsection we outline the control design procedure, however for more details the reader is referred to [30].

Unlike in the direct adaptation, the core of the indirect adaptation algorithm is the identification error

$$e_3 = y_i - y_p \quad (17)$$

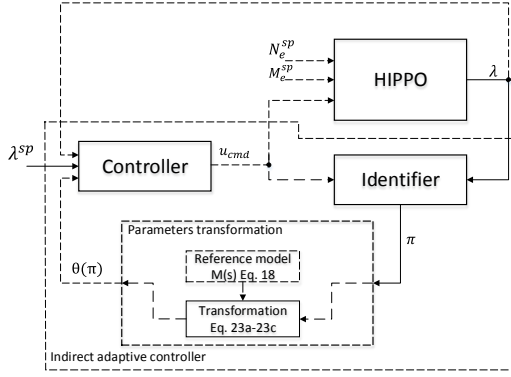


Fig. 7. Indirect adaptive control algorithm block-diagram. Designations:  $N_e^{sp}$  — engine speed set-point,  $M_e^{sp}$  — load torque set-point.

where  $y_i$  is the identified output. The plant is identified using the identification procedure of choice and the identified parameters are used to construct the controller. The plant identified parameters are assumed to be the true ones (the certainty equivalence principle). We demonstrate the algorithm implementation based on the second-order reference model ( $n = 2$ ) with a relative degree 1

$$M(s) = \frac{n_m(s)}{d_m(s)} = \frac{\omega^2 s + 1}{s^2 + 2\zeta\omega s + \omega^2}, \quad (18)$$

which is chosen to be stable and minimum-phase as in case of direct adaptation scheme and  $\omega$  and  $\zeta$  are the design parameters.

The controller design starts by defining the identifier which is known as an equation error identifier [32]. It estimates the process parameters in a specific parametrization (no physical interpretation)

$$\boldsymbol{\pi}^T = [\mathbf{a}^T \mathbf{b}^T] = [a_1 \ a_2 \ b_1 \ b_2], \quad (19)$$

which are used to calculate the process identified output  $y_i = \boldsymbol{\pi}^T \tilde{\mathbf{w}}$ , where  $\tilde{\mathbf{w}} = [w_1^{(1)} \ w_2^{(1)} \ w_1^{(2)} \ w_2^{(2)}]^T \in \mathbb{R}^4$ .

The controller internal signals  $\dot{\mathbf{w}}^{(1)}$  and  $\dot{\mathbf{w}}^{(2)}$  are defined in [30] as

$$\begin{aligned} \dot{\mathbf{w}}^{(1)} &= \mathbf{\Xi} \mathbf{w}^{(1)} + \mathbf{b}_\xi u \\ \dot{\mathbf{w}}^{(2)} &= \mathbf{\Xi} \mathbf{w}^{(2)} + \mathbf{b}_\xi y_p, \end{aligned} \quad (20)$$

which are the first order low-pass filters.

The design parameters  $\mathbf{\Xi} \in \mathbb{R}^{2 \times 2}$  and  $\mathbf{b}_\xi \in \mathbb{R}^2$  have to be chosen in controllable canonical form [30], such that

$$\xi(s) = \det(sI - \mathbf{\Xi}) \quad (21a)$$

$$\xi_0(s) = \xi(s)/n_m(s) \quad (21b)$$

where  $\xi(s)$  is Hurwitz.

The control signal is calculated as

$$u = \boldsymbol{\theta}^T \mathbf{w}$$

with the vector of parameters  $\boldsymbol{\theta}$  and regression vector  $\mathbf{w}$  defined as

$$\begin{aligned} \boldsymbol{\theta}^T &= [c_0 \ \mathbf{c}^T \ \mathbf{d}^T] = [c_0 \ c_1 \ c_2 \ d_1 \ d_2] \in \mathbb{R}^5 \\ \mathbf{w}^T &= [r \ \mathbf{w}^{(1)T} \ \mathbf{w}^{(2)T}] \in \mathbb{R}^5, \end{aligned}$$

where vector  $\boldsymbol{\theta}$  is obtained from vector  $\boldsymbol{\pi}$  in the parameters' transformation block (Fig. 7). The transformation is assumed to be done instantaneously and the procedure is outlined hereafter. First, the time-varying polynomials  $a(s)$ ,  $b(s)$ ,  $c(s)$  and  $d(s)$  are defined to be of  $n-1$  order

$$\begin{aligned} a(s) &= a_1 + a_2 s & c(s) &= c_1 + c_2 s \\ b(s) &= b_1 + b_2 s & d(s) &= d_1 + d_2 s, \end{aligned} \quad (22)$$

where  $a_i(t)$ ,  $b_i(t)$ ,  $c_i(t)$  and  $d_i(t)$  are time-varying coefficients, although time-dependency (t) is omitted to prevent mixing time and frequency domains.

The transformed coefficients  $c_1, c_2, d_1$  and  $d_2$  can now be obtained with the following polynomials [30]

$$c(s) = \xi(s) - \frac{1}{a_2} q(s) a(s) \quad (23a)$$

$$d(s) = \frac{1}{a_2} (q(s) \xi(s) - q(s) b(s) - \xi_0 d_m(s)) \quad (23b)$$

$$c_0 = \frac{k_m}{a_2}, \quad (23c)$$

where the quotient  $q(s)$  is  $n-1$  order polynomial defined as

$$q(s) = \frac{\xi_0(s) d_m(s)}{\xi(s) - b(s)} \quad (24)$$

**Note:** the simulation has shown that the  $a_2$  parameter tends to drift to zero with time. Therefore, it will eventually result into a division by zero in Eqn. 23a, 23b, 23c and the output of the controller will become not a number (NaN). This might go unnoticed if the simulation time is not long enough, but will become an issue once the controller is deployed to the real process. Hence, the parameter  $a_2$  must always be bounded away from zero, which is guaranteed by the following condition

$$\text{if } a_2 = a_{min} \text{ and } \dot{a}_2 < 0 \text{ reset } \dot{a}_2 = 0.$$

It is noted that the transformation of the parameters outlined above is not straightforward for implementation. Therefore, the algorithm for practical implementation is derived in Appendix A.

The parameters adaptation law is a gradient decent algorithm extended with a leakage term as in the case of direct adaptation

$$\dot{\boldsymbol{\pi}} = -\gamma e_3 \tilde{\boldsymbol{w}} - \boldsymbol{\sigma} \boldsymbol{\pi}, \quad (25)$$

where  $\gamma$  is the tuning parameter (aggressiveness).

#### 4 Simulation study

Before deploying the developed controllers to the testbed, we evaluate their performance via numerical simulation. Apart from the nominal stability, the goal is to demonstrate that the controllers remain stable in the presence of drifting parameters in the controlled process. The parameter drift can be caused by various reasons, starting with the changing engine operating conditions (e.g., cold-start, part load, full load) and ending with the components (e.g., sensors, actuators, valves) mechanical wear and tear over time.

In the simulation test case scenario the hybrid engine was run at the constant speed 1600 rpm and the load step changes were applied: 500  $\rightarrow$  300 (Nm) at 215 sec and 300  $\rightarrow$  500 (Nm) at 230 sec. The goal was to track the lambda set-point 3.1 and to reject the load disturbance. As mentioned earlier, the induction motor was used in torque control mode and did not affect the rotational speed of the powertrain.

To evaluate the performance of the designed adaptive controllers, each of them was at first tested under the nominal plant conditions. As it is known that adaptive controllers can exhibit instability even after the initial parameters convergence, the simulation time was chosen long enough to account for that. In addition, the aggressive load variation was applied. As a result, a few robust modifications to each controller were done as described in Section 3.

The adaptive control concepts were justified via simulations with the altered process parameters. In this case the lambda sensor time-delay was assumed to be abruptly increased 0.79  $\rightarrow$  2.29 sec due to sensor wear. It should be noted that such a considerable increase in sensor delay is likely to be alarmed by the on-board diagnosis system for replacement. However, the main purpose of the adaptive control system is to provide sufficient engine performance despite possible components degradation until they can be maintained.

Fig. 8 shows the comparison of the adaptive and fixed parameters control performance under the nominal and degraded sensor conditions. It can be seen that adaptive controllers behave very similarly under both conditions, while the FPC starts to oscillate when the time-delay is increased. We note that the FPC

transient response is more aggressive in the nominal case as compared to the adaptive controllers. It could be de-tuned in order to remain stable under the increased measurement time-delay, however the original response then becomes unacceptably slow.

It can be seen (Fig. 8) that the adaptive control technique is capable of adapting the controller parameters in such a way as to keep the predefined performance of the control system despite the variation of the plant parameters (measurement time-delay). In this work the time-delay was not explicitly included in the linear reference models in order the controller complexity to remain low and be feasible for the testbed implementation. As the rigorous mathematical proof of the stability of adaptive control system applied to a nonlinear system with time-varying delay is a non-trivial task, we verify the designed control systems via experiments.

#### 5 Experimental study

Since the desired controllers behavior has been achieved in the numerical simulation, these results can now be experimentally verified. The HIPPO testbed, where all the measurements and experiments were performed, is shown in Fig. 10.

The performance of the designed controllers is evaluated with two test case scenarios:

1. The mild load variation 400  $\rightarrow$  300  $\rightarrow$  400 (Nm) is applied.
2. The more aggressive load variation 500  $\rightarrow$  300  $\rightarrow$  500 (Nm) is applied.

In both scenarios the engine was run at 1600 rpm and the AFR reference  $\lambda_{ref} = 3.1$  was tracked. The results of the AFR control for the cases 1 and 2 are shown in Fig. 9 and Fig. 11, respectively. In addition, the applied load and the frequency inverter control signal are shown. The load profile uneven shape is explained by the water-brake behavior which introduces little oscillations and irregularities to the generated torque. The AFR identification for the indirect adaptive control scheme is shown in Fig. 13.

Fig. 12 demonstrates the torque developed by the engine, motor and the water-brake during the load transients for the nominal value of the oxygen sensor delay.

By comparing Fig. 8 and Fig. 11 we can see that the experimental results closely resemble the numerical simulations allowing us to rely on the developed hybrid engine model for further powertrain analysis and control.

In each case, the controllers are evaluated under the nominal and altered process parameters. It can be visually observed that the increased time-delay affects neither the adaptive controllers nor the FPC when the load variation is mild (Fig. 9), whereas it does have an

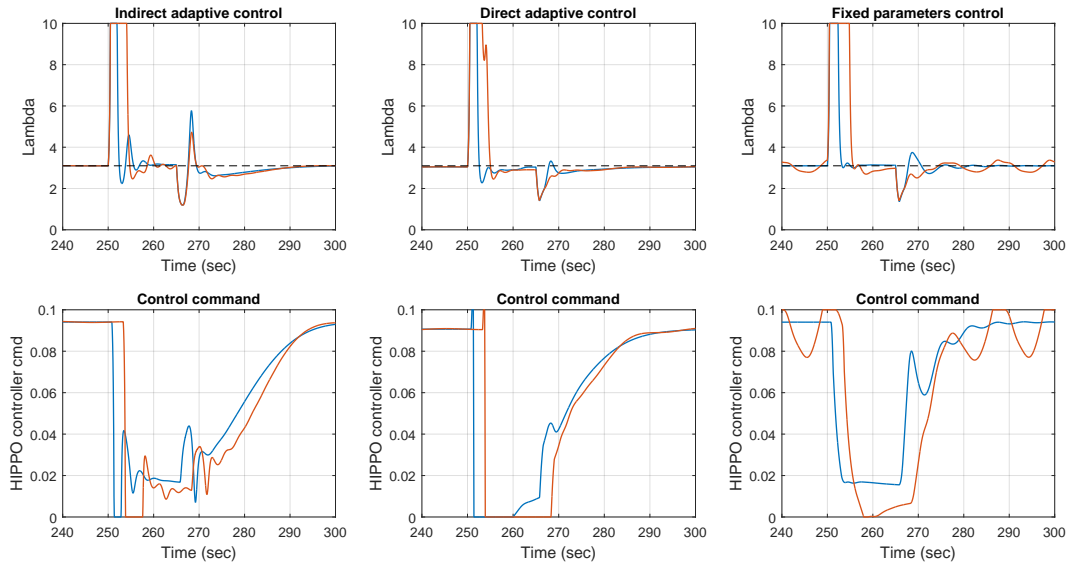


Fig. 8. Simulation study of the adaptive controllers. Lambda set-point tracking  $\lambda = 3.1$  during load step-change. Nominal and measurement delay cases are compared. Load step change  $500 \rightarrow 300$  (Nm) is done at 250 sec and  $300 \rightarrow 500$  (Nm) at 265 sec. Legend: — nominal case, — measurement delay, - - - lambda set-point.

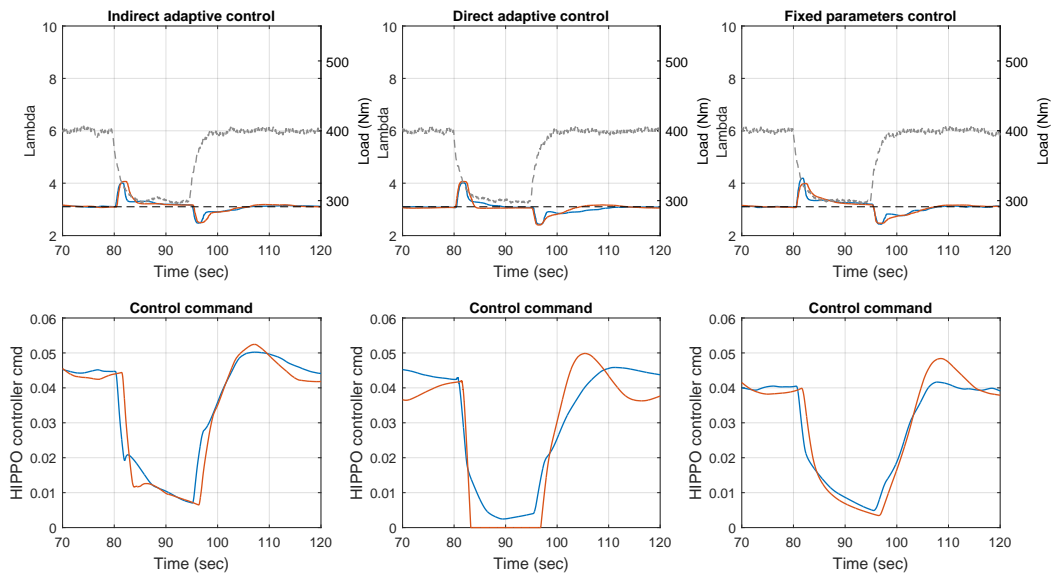


Fig. 9. Experimental verification of the adaptive controllers. Lambda set-point tracking  $\lambda = 3.1$  during mild load step-change  $400 \rightarrow 300 \rightarrow 400$  (Nm). Nominal and measurement delay cases are compared. Load step change  $400 \rightarrow 300$  (Nm) is done at 80 sec and  $300 \rightarrow 400$  (Nm) at 95 sec. Legend: — nominal case, — measurement delay, - - - load, - - - lambda set-point.

impact on their performance when the load variation is large (Fig. 11).

Therefore, for the case 2 we record the controllers time-domain characteristics, including settling time, overshoot and peak, under the nominal and degraded sensor conditions. The characteristics are summarized in Tab. 3. It can be seen that the increase of the measurement time-delay slightly deteriorates the performance of adaptive controllers, causing the settling time to increase by approximately 4 sec for OA and IA algorithms. In addition, the lambda overshoot for these

controllers grows by about 3% and 5.5 %, respectively. However, the FPC fails to maintain the desired performance and starts to oscillate.

The engine-out  $NO_x$  emissions with the AFR closed-loop control has been measured during aggressive load transients. Fig. 14 demonstrates the comparison of the measured  $NO_x$  emissions for the case of degraded UEGO sensor when the adaptive and fixed parameters controllers are online. It is seen that unloading of the engine results into emissions reduction as expected. In addition, the AFR set-point tracking with

Table 3. Experimental study. Controllers behavior after the change in the oxygen sensor time-constant. Tracking the reference  $\lambda = 3.1$ . FPC — fixed parameters control, DA — direct adaptive, IA — indirect adaptive.

Time delay	Controller	FPC	DA	IA
$\tau = 0.79$ (sec)	Rise time (sec)	4.40	28.65	8.50
	Settling time (sec)	22.91	21.58	23.63
	Overshoot (%)	4.00	0.07	3.21
	Peak value	3.22	3.05	3.19
$\tau = 2.29$ (sec)	Rise time (sec)	4.50	6.34	8.50
	Settling time (sec)	oscillating	25.20	27.46
	Overshoot (%)	10.42	3.25	8.96
	Peak value	3.42	3.14	3.31



Fig. 10. Hybrid integrated propulsion powertrain on which all the measurements and experiments presented in the paper are performed. Caterpillar 3176B (dark yellow), water-brake (dark green) and the induction motor (gray) are shown. The cardan shafts connecting the powertrain are covered with the yellow colored casings.

adaptive controllers provides better  $NO_x$  regulation in comparison to the FPC control thereby supporting the idea of the control parameters adaptation.

## 6 Conclusion

In this article the adaptive control algorithms were shown to successfully deal with the unexpected variation of the parameters in the hybrid marine diesel engine. The direct and indirect forms of MRAC algorithms were designed and their performance was evaluated.

First, the developed controllers have been assessed in a simulation environment using the validated mean value model of the hybrid engine. Extensive simulations have shown that a need of more robust concepts exists. The so-called sigma modification was done to both algorithms to increase their robustness. Furthermore, the anti-windup “dead-zone”-like mechanism was added to the direct adaptation scheme in order to stop the adaptation during the control saturation.

Thereafter, the designed controllers were validated with the on-engine tests on the hybrid diesel engine testbed. The benefits of using the adaptive control algorithms were demonstrated by conducting experiments in which the engine parameters changed over time. This change was done by artificially increasing the measurement time-delay of the exhaust gas oxygen sensor. Both adaptive control algorithms were able to keep the predefined control system performance with only minor deterioration. At the same time the controller with fixed parameters showed oscillatory response significantly degrading the overall engine performance.

It can be concluded, that controller parameters adaptation to the varying engine dynamics is an important feature which allows to keep the predefined engine performance and should be therefore considered during the control system design. Eventually, control adaptation prevents increased formation of engine-out emissions, thus reducing the negative impact of engines on the environment.

## Acknowledgments

The authors are grateful to the EU project HERCULES 2, funded by the European Commission, for funding the research and the corresponding author’s visit to the NTUA, Athens. Mr. S. Topaloglou is supported through a grant by the Det Norske Veritas Classification Society (KA 622905) which is gratefully acknowledged.

## Nomenclature

### Physical and geometrical quantities

$M$	torque, Nm
$u_{cmd}$	frequency inverter command, V
$K$	motor model gain
$\tau_{ac}$	motor model time-constant
$R$	specific gas constant, $J \cdot kg^{-1} K^{-1}$

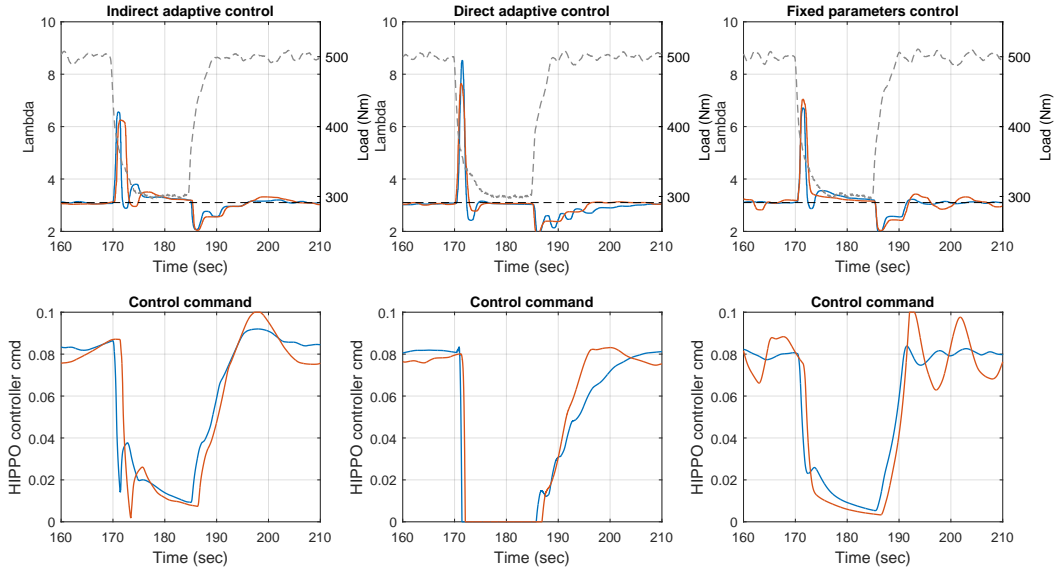


Fig. 11. Experimental verification of the adaptive controllers. Lambda set-point tracking  $\lambda = 3.1$  during aggressive load step-change  $500 \rightarrow 300 \rightarrow 500$  (Nm). Nominal and measurement delay cases are compared. Load step change  $500 \rightarrow 300$  (Nm) is done at 170 sec and  $300 \rightarrow 500$  (Nm) at 185 sec. Legend: — nominal case, — measurement delay, - - - load, - - - lambda set-point.

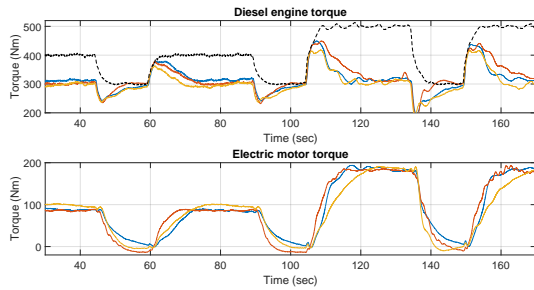


Fig. 12. Experimental verification of the adaptive controllers. Torque curves for diesel engine and electric motor are shown for the designed controllers during lambda set-point tracking  $\lambda = 3.1$ . Legend: — fixed parameters controller, — direct adaptive, — indirect adaptive, - - - load.

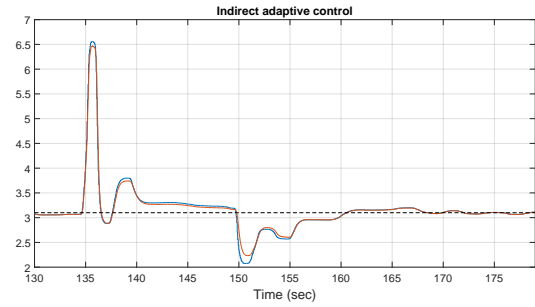


Fig. 13. Experimental results. Lambda online identification. Legend: — measured lambda, — online identified lambda, - - - lambda set-point.

T temperature, K

V manifold volume,  $m^{-3}$

$c_{p,i}$  gas specific heat constant,  $J \cdot kg^{-1} K^{-1}$

$\gamma_c = c_{p,i}/c_{v,i}$  specific heat ratio

$\mu_c = (\gamma_c - 1)/\gamma_c$  constant

P power, W

W mass flow, kg/s

$\lambda$  air-fuel ratio

$V_d$  engine displacement volume,  $m^{-3}$

$\eta$  efficiency, %

$\omega_e$  engine speed,  $rad/s$

A area,  $m^2$

$\psi()$  flow correction coefficient

$r_c = \left(\frac{2}{\gamma+1}\right)^{\frac{\gamma}{\gamma-1}}$  critical pressure ratio

J mass moment of inertia,  $kg \cdot m^2$

$H_i$  lower heating value of the fuel, MJ/kg

$f_{mep}$  friction mean effective pressure, kPa

$\bar{S}_p = 2SN_e/60$  mean piston speed, m/s

S stroke, m

$N_e$  engine rotational speed, rpm

### Subscripts

ac alternating current

cmd command

i intake

x exhaust

f fuel

c compressor

xt turbine

a ambient

is isentropic

e engine

l load

fr friction

s stoichiometric

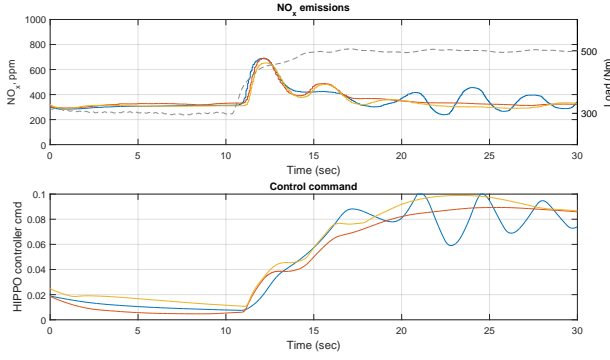


Fig. 14. Experimental study. Measured  $NO_x$  emissions with the AFR closed-loop control and degraded UEGO sensor. Legend (top plot):

— fixed parameters control, — output adaptive control, — indirect adaptive control, - - - load.

### Abbreviations

IMO international Maritime Organization  
 PTO power take out  
 PTI power take in  
 UEGO universal exhaust gas oxygen  
 HIPPO hybrid integrated propulsion powertrain

### A Practical implementation of the parameters transformation for the indirect adaptive control algorithm

Here we derive the equations for the time-varying coefficients defined in Eqn. 22 which are straightforward for implementation in Simulink. The equations are derived for the model defined in Eqn. 18 with  $\omega = 1$  and  $\zeta = 1$ .

It is seen from Eqn. 24 that the quotient  $q(s)$  is a first order monic polynomial

$$q(s) = s + q_0. \quad (26)$$

Taking into account Eqn. 24

$$(s + q_0)(\xi(s) - b(s)) = \xi_0(s)d_m(s)$$

Inserting the expressions for  $\xi(s)$ ,  $b(s)$ ,  $\xi_0(s)$  and  $d_m(s)$ , which are defined in Eqn. 21a, 22, 21b and 18, respectively, the Diophantine equation can be written as

$$s^3 + 3s^2 + 3s + 1 = s^3 + (2 - b_2 + q_0)s^2 + (1 - b_1 + q_0(2 - b_2))s + q_0(1 - b_1) \quad (27)$$

In order the  $q(s)$  to be the first order polynomial we have to equate the coefficients of  $s^3$  and  $s^2$  of Eqn. 27.

This yields

$$(2 - b_2 + q_0) = 3 \Rightarrow q_0 = 1 + b_2 \quad (28)$$

The polynomial  $c(s)$  is defined in Eqn. 23a. Inserting polynomials for  $\xi(s)$ ,  $q(s)$  and  $a(s)$ , which are defined in Eqn. 21a, 26 and 22, respectively, the  $c(s)$  polynomial coefficients can be obtained

$$c(s) = \underbrace{\left(2 - \frac{a_1}{a_2} - q_0\right)}_{c_2} s + \underbrace{\left(1 - q_0 \frac{a_1}{a_2}\right)}_{c_1} \quad (29)$$

The polynomial  $d(s)$  is defined in 23b. Inserting polynomials for  $\xi(s)$ ,  $q(s)$ ,  $b(s)$ ,  $\xi_0(s)$  and  $d_m(s)$ , which are defined in Eqn. 21a, 26, 22, 21b and 18, respectively, the  $d(s)$  polynomial coefficients can be obtained

$$d(s) = \underbrace{\frac{1}{a_2}(-2 - b_1 + (2 - b_2)q_0)}_{d_2} s + \underbrace{\frac{1}{a_2}(q_0 - b_1 - 1)}_{d_1} \quad (30)$$

The expressions for the coefficients of the time-varying polynomials can now be summarized as

$$\begin{array}{ll} q_0 = 1 + b_2 & d_1 = (b_2 - b_1)/a_2 \\ c_1 = 1 - \frac{a_1}{a_2} - b_2 \frac{a_1}{a_2} & d_2 = (b_2 - b_1 - b_2^2)/a_2 \\ c_2 = 1 - b_2 - \frac{a_1}{a_2} & \end{array} \quad (31)$$

The Eqn. 31 shows that the transformation  $\pi(t) \Rightarrow \theta(\pi)$ , in fact, consists of fixed number of simple mathematical operations (division, multiplication, addition).

### References

- [1] International maritime organization, nitrogen oxides (nox) regulation 13. See also URL <http://www.imo.org>.
- [2] Higher efficiency, reduced emissions, increased reliability and lifetime, engines for ships, 2012. See also URL <http://hercules-c.com>.
- [3] Fuel flexible, near -zero emissions, adaptive performance marine engine, 2015. See also URL <http://cordis.europa.eu>.
- [4] Sciarretta, A., and Guzzella, L., 2007. "Control of hybrid electric vehicles". *Control systems, IEEE*, 27(2), pp. 60–70.
- [5] Wirasingha, S. G., and Emadi, A., 2011. "Classification and review of control strategies for plug-in hybrid electric vehicles". *vehicular Technology, IEEE Transactions on*, 60(1), pp. 111–122.

- [6] Borhan, H., Vahidi, A., Phillips, A. M., Kuang, M. L., Kolmanovsky, I. V., and Cairano, S. D., 2012. "Mpc-based energy management of a power-split hybrid electric vehicle". *Control Systems Technology, IEEE Transactions on*, **20**(3), pp. 593–603.
- [7] Kim, N., Cha, S., and Peng, H., 2011. "Optimal control of hybrid electric vehicles based on pontryagin's minimum principle". *Control Systems Technology, IEEE Transactions on*, **19**(5), pp. 1279–1287.
- [8] Stockar, S., Marano, V., Rizzoni, G., and Guzzella, L., 2010. "Optimal control for plug-in hybrid electric vehicle applications". In American Control Conference (ACC), 2010, IEEE, pp. 5024–5030.
- [9] Piccolo, A., Ippolito, L., Galdi, V. Z., and Vaccaro, A., 2001. "Optimisation of energy flow management in hybrid electric vehicles via genetic algorithms". In Advanced Intelligent Mechatronics, 2001. Proceedings. 2001 IEEE/ASME International Conference on, Vol. 1, IEEE, pp. 434–439.
- [10] Hountalas, D., and Kouremenos, A., 1999. "Development and application of a fully automatic troubleshooting method for large marine diesel engines". *Applied Thermal Engineering*, **19**(3), pp. 299–324.
- [11] Dedes, E. K., Hudson, D. A., and Turnock, S. R., 2012. "Assessing the potential of hybrid energy technology to reduce exhaust emissions from global shipping". *Energy Policy*, **40**, pp. 204–218.
- [12] Nielsen, K. V., Blanke, M., and Vejlgaard-Laursen, M., 2015. "Nonlinear adaptive control of exhaust gas recirculation for large diesel engines". *IFAC-PapersOnLine*, **48**(16), pp. 254–260.
- [13] Tang, H., Weng, L., Dong, Z. Y., and Yan, R., 2009. "Adaptive and learning control for si engine model with uncertainties". *Mechatronics, IEEE/ASME Transactions on*, **14**(1), pp. 93–104.
- [14] Muske, K. R., Jones, J. C. P., and Franceschi, E., 2008. "Adaptive analytical model-based control for si engine air–fuel ratio". *Control Systems Technology, IEEE Transactions on*, **16**(4), pp. 763–768.
- [15] Liu, D., Javaherian, H., Kovalenko, O., and Huang, T., 2008. "Adaptive critic learning techniques for engine torque and air–fuel ratio control". *Systems, Man, and Cybernetics, Part B: Cybernetics, IEEE Transactions on*, **38**(4), pp. 988–993.
- [16] Wang, S., Yu, D., Gomm, J., Page, G., and Douglas, S., 2006. "Adaptive neural network model based predictive control for air–fuel ratio of si engines". *Engineering Applications of Artificial Intelligence*, **19**(2), pp. 189–200.
- [17] Larguech, S., Aloui, S., Pagès, O., El Hajjaji, A., and Chaari, A., 2016. "Fuzzy sliding mode control for turbocharged diesel engine". *Journal of Dynamic Systems, Measurement, and Control*, **138**(1), p. 011009.
- [18] Samokhin, S., and Zenger, K., 2014. "Robust and adaptive wastegate control of turbocharged internal combustion engines". In American Control Conference (ACC), 2014, IEEE, pp. 3219–3224.
- [19] Sciberras, E., and Norman, R., 2012. "Multi-objective design of a hybrid propulsion system for marine vessels". *Electrical Systems in Transportation, IET*, **2**(3), pp. 148–157.
- [20] Clegg, B., Griffiths, H., Hall, D., and Tavner, P., 1999. "The application of drives and generator technology to a modern container ship". In Electrical Machines and Drives, 1999. Ninth International Conference on (Conf. Publ. No. 468), IET, pp. 312–316.
- [21] Ling, P., Yongdong, L., Jianyun, C., and Guofeng, Y., 2007. "Vector control of a doubly fed induction generator for stand-alone ship shaft generator systems". In Electrical Machines and Systems, 2007. ICEMS. International Conference on, IEEE, pp. 1033–1036.
- [22] Van Basshuysen, R., and Schäfer, F., 2004. *Internal combustion engine handbook-basics, components, systems and perspectives*, Vol. 345.
- [23] Dimopoulos, G. G., Georgopoulou, C. A., Stefanatos, I. C., Zymaris, A. S., and Kakalis, N. M., 2014. "A general-purpose process modelling framework for marine energy systems". *Energy Conversion and Management*, **86**, pp. 325–339.
- [24] Malkhede, D. N., Seth, B., and Dhariwal, H., 2005. Mean value model and control of a marine turbocharged diesel engine. Tech. rep., SAE Technical Paper.
- [25] Jung, M., and Glover, K., 2006. "Calibratable linear parameter-varying control of a turbocharged diesel engine". *Control Systems Technology, IEEE Transactions on*, **14**(1), pp. 45–62.
- [26] Guzzella, L., and Amstutz, A., 1998. "Control of diesel engines". *Control Systems, IEEE*, **18**(5), pp. 53–71.
- [27] Wahlström, J., 2006. "Control of egr and vgt for emission control and pumping work minimization in diesel engines".
- [28] Jankovic, M., and Kolmanovsky, I., 1998. "Robust nonlinear controller for turbocharged diesel engines". In American Control Conference, 1998. Proceedings of the 1998, Vol. 3, IEEE, pp. 1389–1394.
- [29] Heywood, J. B., 1988. *Internal combustion engine fundamentals*, Vol. 930. Mcgraw-hill New York.
- [30] Sastry, S., and Bodson, M., 2011. *Adaptive control: stability, convergence and robustness*. Courier Corporation.
- [31] Ioannou, P. A., and Sun, J., 2012. *Robust adaptive control*. Courier Corporation.
- [32] Ljung, L., 1998. *System identification*. Springer.